



**BRNO UNIVERSITY OF TECHNOLOGY**

VYSOKÉ UČENÍ TECHNICKÉ V BRNĚ

**CENTRAL EUROPEAN INSTITUTE OF TECHNOLOGY BUT**

STŘEDOEVROPSKÝ TECHNOLOGICKÝ INSTITUT VUT

**DAMAGE MECHANISMS IN NICKEL-BASED SUPERALLOY  
RENÉ 41 SUBJECTED TO FATIGUE**

MECHANISMY POŠKOZENÍ NIKLOVÉ SUPERSLITINY RENÉ 41 PŘI ÚNAVĚ

**DOCTORAL THESIS SUMMARY**

TEZE DIZERTAČNÍ PRÁCE

**AUTHOR**

AUTOR PRÁCE

**Ing. Tomáš Babinský**

**SUPERVISOR**

ŠKOLITEL

**prof. RNDr. Jaroslav Polák, DrSc.**

**BRNO 2023**



## Abstrakt

Předkládaná práce se zabývá vznikem poškození ve tvářené niklové superslitině René 41, která je podrobena únavovému zatěžování za pokojové a zvýšené (800 °C) teploty. Slitina byla zkoumána ve dvou termodynamických stavech: po rozpouštěcím žhání a po stárnutí. Jednoosé zkoušky nízkocyklové únavy byly prováděny symetricky vzhledem k řízené veličině, kterou byla celková podélná deformace. Za účelem studia mechanismů poškození a jejich souvislosti s plastickou deformací byly aplikovány techniky elektronové mikroskopie doplněné o analýzu cyklické odezvy ve formě hysteretických smyček statistickým přístupem. Navíc byly provedeny přerušované únavové zkoušky za účelem studia vývoje povrchového reliéfu ve vztahu k dislokační substruktuře, k čemuž bylo opět využito elektronové mikroskopie. Porušení za pokojové teploty bylo povětšinou transkrystalické, únavové trhliny iniciovaly především uvnitř zrn z povrchového reliéfu. Srovnáme-li dva zkoušené stavy, stárnutý materiál vykazoval vyšší hodnoty cyklického napětí a při srovnatelném napětí dosahoval vyšších životností. Cyklická deformace byla od prvního cyklu lokalizována do persistentních skluzových pásů. Bylo zjištěno, že většina skluzových pásů vzniká na začátku únavového života, kvůli čemuž jsou koherentní precipitáty  $\gamma'$  významně deformovány pouze na začátku únavového života. Skluz v persistentních skluzových pásech vedl k vytvoření povrchového reliéfu ve formě skluzových schodů, extruzí a intruzí. Vznik povrchového reliéfu byl podrobně diskutován s existujícími modely. Vysokoteplotní expozice měla za následek oxidaci povrchu, zejména na oslabených hranicích zrn, kde iniciovaly a následně se šířily únavové trhliny. Výsledné poškození bylo tudíž interkrystalické.

## Klíčová slova

Nízkocyklová únava, Lokalizace cyklické deformace, Persistentní skluzový pás, Persistentní skluzová stopa, Dislokace, Elektronová mikroskopie, Superslitina

## **Abstract**

The present study deals with the aspects of fatigue damage in a wrought Ni-based superalloy René 41. The material of interest was investigated in two thermodynamical states: solutionised and aged. Uniaxial, fully-reversed low-cycle fatigue tests were conducted at room and elevated (800 °C) temperatures under total strain amplitude control. To study the relevant damage mechanisms and reveal their connection to plastic deformation, a detailed analysis of the cyclic response using a statistical approach was performed, and advanced microscopy techniques were employed, namely scanning and transmission electron microscopy. Interrupted fatigue tests were performed to study the evolution of surface relief and the underlying dislocation structure. After each interruption, the evolution of the microstructure was analysed using electron microscopy techniques. At room temperature, the damage was mostly transgranular, and the cracks initiated predominantly within grains from the roughened surface. Comparing the two investigated material states, the aged material attained higher stresses and exhibited higher lifetimes in service-relevant stress-life relation. Cyclic deformation was found to localize to persistent slip bands since the first cycle, and the majority of slip bands formed very early in the fatigue life. Hence, shearing of the strengthening phase, coherent  $\gamma'$  precipitates, occurred largely only in the first few cycles. Due to the cyclic slip localization, surface roughening emanated in the form of slip steps, extrusions and intrusions. The formation of surface relief was thoroughly discussed with existing models. The exposure to high temperatures led to an environmental attack, due to which an oxide layer formed on the surface. The cracks initiated and propagated along weakened grain boundaries, and the resulting damage was thus intergranular.

## **Keywords**

Low-cycle fatigue, Cyclic slip localization, Persistent slip band (PSB), Persistent slip marking (PSM), Dislocation, Electron microscopy, Superalloy

# Table of contents

1	Introduction .....	6
2	Aims of the thesis .....	7
3	Experimental .....	8
3.1	Material – Ni-based superalloy René 41 .....	8
3.2	Methods .....	8
3.2.1	Test specimen preparation .....	8
3.2.2	Mechanical testing and data analysis .....	9
3.2.2.1	Interrupted fatigue tests .....	9
3.2.3	Electron microscopy observation .....	10
3.2.3.1	SEM observation .....	10
3.2.3.2	FIB cross-sections and preparation of lamellae for TEM observation.....	10
3.2.3.3	TEM observation.....	11
4	Selected results and discussion .....	12
4.1	Lifetime and damage .....	12
4.1.1	Room temperature fatigue loading .....	12
4.1.2	High temperature (800 °C) fatigue loading.....	13
4.2	Analysis of cyclic deformation behaviour .....	17
4.2.1	Room temperature fatigue loading .....	17
4.2.2	High temperature (800 °C) fatigue loading.....	18
4.3	Evolution of surface relief and the underlying microstructure .....	21
5	Conclusions .....	24
6	References .....	25
7	List of publications by the author.....	27

# 1 Introduction

Along with the development of materials science since the 19<sup>th</sup> century, several fields of science dedicated to specific problems arose in time. The need for materials able to withstand many years of service led to the research of premature cracks and the fatigue damage causing them. Thus, fatigue damage is of the utmost importance for the material design of various mechanical components. Fatigue refers to the changes in properties and microstructure due to the applied repeated loading. The key feature of research in the area of fatigue damage is the description of fundamental mechanisms taking place in any material under the conditions of fatigue loading.

According to the most widespread approach, we distinguish two major areas of fatigue life: *low-cycle* and *high-cycle fatigue*, which are separated by a limit of  $10^5$  cycles. Whereas researchers studying fatigue life of mechanical parts supposed to withstand a huge number of cycles, e.g. in the automotive industry, focus on high-cycle fatigue, researchers studying limits of extremely thermally exposed materials, e.g. in jet engines during take-off/landing procedure, focus on low-cycle fatigue. Low-cycle fatigue corresponds to extreme loading conditions above the yield limit of the material, which results in severe damage throughout the component. Even though the mechanisms of high-cycle fatigue may vary significantly, the basic mechanisms of low-cycle fatigue are also valid for the high-cycle fatigue domain as well. The operating mechanisms are dependent not only on the experimental conditions but also on the applied stress or strain. The number of cycles until fracture is generally the higher the less plasticity is induced in a material. The role of plastic strain in cyclic damage was independently clarified by Coffin (1954) and Manson (1953). The formulated empirical Coffin-Manson's law marks the beginning of a systematic investigation of the aspects of cyclic plasticity and is still the most used approach for the assessment of the cyclic plastic behaviour of materials.

Although the fundamental fatigue mechanisms have been explained quite well in simple metals such as pure copper or aluminium, the fundamental mechanisms acting in engineering materials with complex microstructures such as nickel-based superalloys are less clear. This is crucial for better understanding of material behaviour under real operating conditions, and eventually more precise fatigue-life estimations of relevant components. Nickel-based superalloys are commonly used for manufacturing of hot-going components for almost a century. A typical example of application are turbine blades and vanes in aircraft engines, emphasizing the essential role superalloys play, for instance, in air travel or energy conversion. The excellent high-temperature performance is closely related to the unique microstructure of superalloys, typically exhibiting a large volume fraction of coherent precipitates embedded in the matrix. It is, however, unclear to this day how exactly this unique microstructure affects the evolution of fatigue damage. Such fundamental relationship is possible to assess only with the help of high-resolution imaging techniques such as scanning and transmission electron microscopy.

Hence, in this work, advanced microscopy techniques were employed to study relevant damage mechanisms under cyclic loading in low-cycle regime in the material of choice – nickel-based superalloy René 41.

## 2 Aims of the thesis

The thesis aims to clarify the fundamental damage mechanisms leading to the initiation of cracks in nickel-based superalloys subjected to fatigue loading. The topic of fatigue damage and the initiation of fatigue cracks has been studied for a long time. The case of simple one-phase materials such as pure copper or aluminium is quite well described in a number of sources [1–3], however, the explanations of the observations differ. Several models attempting to cover the physical aspects preceding the fatigue crack initiation have been proposed in past [4–7] but it is still an open topic since the scientific community is not unanimous on it yet.

Engineering materials are usually much more complicated than simple metals in terms of structure, and this directly relates also to the fatigue response of the material and the damage mechanisms responsible for possible premature failure of mechanical components. Even if there are many sources [8–11] discussing the relevant damage mechanisms in complex engineering materials such as nickel-based superalloys, a satisfying explanation dealing with how the fatigue cracks initiate has not yet been presented. The material of interest in this study is a wrought nickel-based superalloy René 41. Although high-cycle fatigue properties of the alloy are known for years [12], material behaviour under high cyclic stresses introducing plastic strains has not been to the author's knowledge comprehensively studied.

The objectives are as-follows:

- characterization of low-cycle fatigue behaviour of a chosen nickel-based superalloy – René 41 – in both solutionised and precipitation-hardened (aged) states,
- comparison of relevant damage mechanisms at room and elevated temperature (800 °C),
- clarification of the influence of the localization of plastic strain on the occurrence of fatigue cracks and fatigue fracture in general,
- finding the relation between the stress-strain response of the material on one hand and the microstructural changes and related damage mechanisms on the other,
- clarification of the role of defects on the fatigue crack initiation in nickel-based superalloys,
- studying the evolution of plastic strain localization into persistent slip bands,
- analysis of cyclic plasticity using the statistical theory of the hysteresis loop.

## 3 Experimental

### 3.1 Material – Ni-based superalloy René 41

René 41 is a precipitation-hardened superalloy which exhibits high strength at high temperatures. It is commonly used in the most thermally exposed parts of jet engines and missile components [13], such as turbine disks or exhaust nozzles, due to its microstructural stability at high temperatures, high corrosion, and creep resistance. According to the technical guide [14], René 41 is commonly used at temperatures up to 760 °C, however, some authors [15] report a use up to 815 °C for long exposures and up to 980 °C for short exposures.

The material tested in the present study was supplied by VDM Metals in the form of a cylindrical bar of 12 mm in diameter. Table 1 shows the chemical composition analysed using optical emission spectroscopy in the as-received state. The material was tested in two thermodynamical states: solutionised, and solutionised and precipitation-hardened, further labelled as aged for the sake of simplicity. Solution heat treatment was performed at 1060 °C for 1 hour, followed by cooling in air. Solution heat treatment was performed to dissolve the undesirable phases and reach a homogeneous distribution of elements and maximum ductility. Precipitation hardening (ageing), introducing the  $\gamma'$  precipitates to the microstructure, was performed following the recommendation from [14] at 760 °C for 16 hours, followed by cooling in air. Specimens for interrupted fatigue testing were aged in a vacuum and cooled in the furnace to achieve a larger precipitate size, which provided better contrast for precipitates in lamellae for TEM observation.

Table 1. Chemical composition of René 41 superalloy measured using optical emission spectroscopy. Note that N content was not evaluated due to the technical limitations of the spectroscope.

	Ni	Cr	Co	Mo	Ti	Al	Fe	C	Si
René 41	53.22	18.30	11.04	10.13	2.90	1.68	1.87	0.07	0.07

## 3.2 Methods

### 3.2.1 Test specimen preparation

Specimens were machined from the bars to a cylindrical shape with the gauge length and diameter of 12 and 6 mm for room-temperature testing, and 15 and 6 mm for high-temperature testing. The gauge length was mechanically ground, polished with a diamond compound (down to a size of 1  $\mu\text{m}$ ) and electrochemically polished to acquire a mirror-like surface suitable for electron microscopy observations. Electropolishing conditions are listed in Table 2. The preparation of a smooth surface of aged René 41 superalloy proved to be challenging as fine Mo-rich carbides at grain boundaries were attacked by an electrolyte primarily. The least damage to the surface was imposed by a solution of methanol, nitric acid and perchloric acid, and it was eventually removed by manual polishing with colloidal silica.

Table 2. Electropolishing conditions.

René 41	Electrolyte (volume ratio)	T [°C]	U [V]	t [s]
Solutionised	93.9 CH <sub>3</sub> CH <sub>2</sub> OH + 1.4 HNO <sub>3</sub> + 4.7 HClO <sub>4</sub>	-16	54	5
Aged	93.9 CH <sub>3</sub> CH <sub>2</sub> OH + 1.4 HNO <sub>3</sub> + 4.7 HClO <sub>4</sub>	5	20	4

### 3.2.2 Mechanical testing and data analysis

Fatigue tests were performed in laboratory air using the computer-controlled servohydraulic testing machine MTS 880. Servohydraulic testing machine MTS 810 with a furnace was utilised for high-temperature testing (up to 1000 °C). Specimens were subjected to fully-reversed, uniaxial cyclic straining ( $R = -1$ ) at a constant strain rate of  $2 \cdot 10^{-3} \text{ s}^{-1}$  at room temperature and elevated temperature of 800 °C, which represents the most demanding conditions for the tested material. The test temperatures were chosen to study relevant cyclic deformation behaviour and fundamental damage mechanisms with and without the high-temperature effect. All tests were performed in strain control with constant total strain amplitude. The total strain amplitudes are listed in Table 3 and were chosen so that the resulting lifetimes approximately cover the range of 500–20000 cycles. The strain was measured longitudinally using an MTS contact axial extensometer for LCF testing. In the case of room temperature tests, the extensometer with a gauge length of 8 mm was attached to the specimen gauge length using metallic springs around the gauge diameter. In the case of high-temperature tests, the extensometer with a gauge length of 12 mm was placed outside the furnace and attached to the specimen gauge length using air-cooled alumina extension rods.

In each cycle, 2000 data points were recorded for data analysis. Data postprocessing, including numerical differentiation of the experimentally obtained hysteresis loops, was performed using the dedicated software Derivace, specifically designed by Jiří Tobiáš. Fatigue lifetime was evaluated using the criterion

$$k_{cr} = \frac{\sigma_m}{\sigma_a} \leq -0.3. \quad (3.1)$$

Analysis of the loop shape was performed using the statistical theory of the hysteresis loop [16]. Experimental curves approximating probability density functions of critical internal stresses were derived from the second derivatives of relative stress to relative strain. In each point, numerical differentiation was performed by establishing the slope of a linear fit of the nearest 15 data points. Afterwards, the data were numerically smoothed by averaging the nearest 70 data points. Second derivatives of tensile and compressive half-loops for selected cycles were plotted in the form of  $-\frac{2}{E_{eff}^2} \frac{\partial^2 \sigma_r}{\partial \varepsilon_r^2}$  against fictive stress in the form  $\frac{\varepsilon_r E_{eff}}{2}$ . Effective moduli  $E_{ef}$  were evaluated for the corresponding cycles. Since the differences in the second derivatives between tensile and compressive half-loops were not substantial (see the full version of the thesis), only the analyses corresponding to compressive half-loops are shown.

Table 3. Fatigue test conditions adopted in the present study.

René 41	T (°C)	$\varepsilon_a$ (%)
Solutionised	23	0.5, 0.8, 1.0, 1.2
Aged	23	0.5, 0.8, 1.0, 1.2
Aged	800	0.23, 0.35, 0.5, 0.8

#### 3.2.2.1 Interrupted fatigue tests

Room-temperature fatigue tests cycled with  $\varepsilon_a = 0.8\%$  were interrupted after the definite number of elapsed cycles to study microstructural changes using electron microscopy. Two types of interruptions were used, as depicted in Fig. 3.1. The solutionised specimen was interrupted at maximum compression strain (see Fig. 3.1a), followed by relaxation of the elastic strain resulting in a stress drop to zero, while the plastic strain remained. The interruptions were performed after 1, 3, 10, 30, 100 and 500 cycles. The cycling after interruption continued from

the end strain level (at zero stress) within the prescribed strain range  $\pm 0.8\%$ . Interruptions to the aged specimen were enhanced as depicted in see Fig. 3.1b. To reach zero plastic strain, the test run was interrupted at a specific total strain, derived from an uninterrupted test run cycled with the identical total strain amplitude of  $\varepsilon_a = 0.8\%$ . The interruptions were performed after 1, 10 and 100 cycles. This approach mitigated the disproportion between compressive and tensile plastic strains which might be significant in the first few cycles.

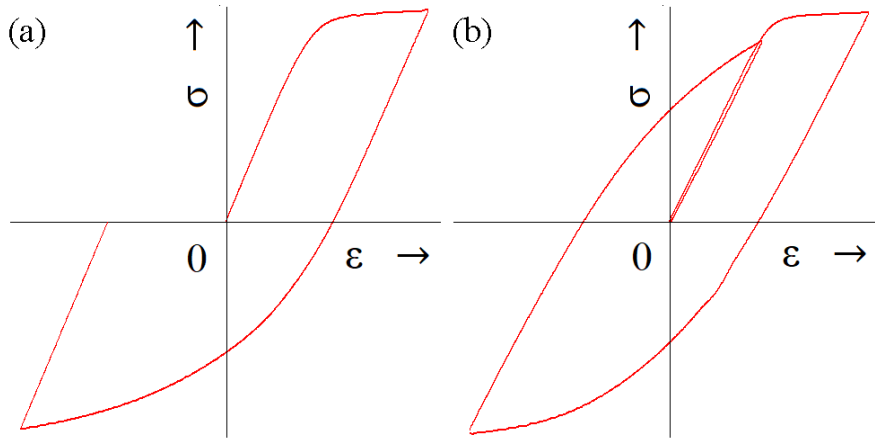


Fig. 3.1. Schematic illustration of the two types of performed interruptions. (a) Interruption at maximum compression strain was adopted for the solutionised specimen. (b) Interruption at 0% strain was adopted for the aged specimen.

### 3.2.3 Electron microscopy observation

#### 3.2.3.1 SEM observation

Specimen surfaces considered for observations using the methods of electron microscopy were carefully polished to acquire mirror-like surfaces. Firstly, the surface was mechanically ground using SiC grinding paper, followed by polishing using diamond compound down to a particle size of  $1\ \mu\text{m}$ , and final mechanical-chemical polishing using colloidal silica with a particle size of  $0.04\ \mu\text{m}$ . Eventually, the specimens were cleaned using an ultrasound cleaning system and Tergeo plasma cleaner.

Electron microscopy techniques were used for a detailed analysis of the initial material state and material after cycling. Overall damage as well as fracture surface and surface relief were observed using scanning electron microscope SEM LYRA 3 XMU FEG/SEM (SEM). The imaging was performed using an electron beam with an accelerating voltage of 10 kV. The SEM was equipped with a focused ion beam (FIB), utilised for cross-sectioning, energy-dispersive x-ray spectroscope Ultimmax (EDS) for local chemical analyses, and electron back-scattered diffraction detector Symmetry (EBSD) with AZtec software for grain size, grain and twin boundary identification and texture evaluation. The grain size and texture analyses using EBSD were performed on square areas of  $1\ \text{mm}^2$  with a step size of  $0.5\ \mu\text{m}$  on specimen cross-sections under the electron beam with an accelerating voltage of 20 kV. Identical voltage was used also for EBSD analysis of grain and twin boundaries at the surface secondary cracks. The secondary crack analysis was performed on longitudinal sections over 2 mm from the fracture surface.

#### 3.2.3.2 FIB cross-sections and preparation of lamellae for TEM observation

FIB with high-energy gallium ions was utilised to mill out shallow cross-sections revealing the microstructural features underneath the specimen surface and to prepare thin lamellae for TEM

observations from the specimen surface. Due to the microscope configuration, the specimens had to be tilted by  $55^\circ$  to produce the cross-sections, causing a distortion of true dimensions in the corresponding SEM micrographs. Both cross-sections and lamellae were oriented parallel to the loading axis (perpendicular to the surface), so the specimen/loading axis always lay in the cross-section/lamella plane. For the sake of uniformity, average-sized grains with a maximum size of  $20\ \mu\text{m}$  and persistent slip markings (PSMs) approximately perpendicular (within a  $15^\circ$  deviation) to the cross-section plane were chosen.

To protect the surface from redeposition and ion damage during milling, a protective Pt layer was deposited by melting the Pt powder, which was then sprayed onto the surface by a gas injection system, using an electron beam and ion beam, subsequently. The electron beam deposition was performed at an accelerating voltage of 5 kV. The ion-beam-induced deposition (accelerating voltage 30 kV, probe current 150–200 pA) was followed by rough milling of the cross-section (30 kV, 4–10 nA), which was subjected to two-step polishing afterwards (rough polishing at 30 kV, 1 nA and smooth polishing at 30 kV, 100–200 pA). The resulting cross-sections were approximately 10–15  $\mu\text{m}$  wide and 10  $\mu\text{m}$  deep.

The lamellae production procedure is an extended version of the production procedure of the cross-sections. The surface was protected by a Pt layer deposited using electron and ion beams, subsequently. Lamellae were prepared by careful FIB milling at both sides of the area of interest, followed by cutting the lamella off the specimen bulk using J-cut, and lifting out *in-situ* using a micromanipulator. Afterwards, the lamellae were attached to a copper TEM grid and thinned down to  $\sim 100\ \text{nm}$  by careful polishing. In addition to the polishing procedure described above, the lamellae were finally polished with low accelerating voltages (5 kV and finally 2 kV) to reduce ion damage and contamination. The resulting lamellae were approximately 10–15  $\mu\text{m}$  wide, 10  $\mu\text{m}$  deep and 100 nm thick.

### 3.2.3.3 TEM observation

Thin foils for TEM observations were prepared *post-mortem* from representative specimens cycled with  $\varepsilon_a = 0.5\%$  using standard procedure. Approximately 3-mm-wide plates were cut from a specimen transversally to the specimen axis and thinned down to  $70\ \mu\text{m}$  by grinding on SiC grinding papers. Consequently, foils were produced from the plates by electrochemical thinning in a double jet device TenuPol2 using an electrolyte consisting of 70 vol.% methanol, 20 vol.% glycerine and 10 vol.% perchloric acid. The electropolishing was performed at 11.5V/-5  $^\circ\text{C}$  until the foil was sufficiently thin for TEM observation ( $\sim 100\ \text{nm}$ ).

TEM technique was adopted for observations of the true surface relief and its relation to the underlying dislocation structure on the site-specific lamellae prepared by FIB, the observations of the dislocation structures and other related microstructural features on thin foils, and for particle analysis and analysis of the specimen crystallography. The presented TEM micrographs were captured in scanning mode (STEM) using JEOL JEM-2100F transmission electron microscope equipped with a double tilt holder and an EDS detector Oxford Instruments X-MAX 80, and Thermo Scientific Talos F200i equipped with a double tilt holder and with built-in EDS detector. Both microscopes were operated at 200 kV. Diffraction patterns and Kikuchi lines were used to determine the crystallographic orientation of the loading axis, foil/lamella, specific grains and related dislocation structures. Dislocation structures were further analysed with three different diffraction vectors. For particle analysis, at least three different diffraction patterns were analysed using the ICSD database of phases and JEMS software, and the connecting Kikuchi lines were compared with projections by JEMS software.

## 4 Selected results and discussion

### 4.1 Lifetime and damage

#### 4.1.1 Room temperature fatigue loading

Lifetime data from the tests conducted at room temperature (RT) are depicted by red and blue colour in Fig. 4.1a–b. Lifetimes were evaluated using the  $k_{cr}$  criterion (Eq. (3.1)). Due to missing saturation plateau, stress amplitude was evaluated at half-life and plastic strain amplitude was derived from the width of the half-life hysteresis loop at mean stress. Fig. 4.1a shows a plot of half-life stress amplitude  $\sigma_{a,50\%N_f}$  vs. double lifetime  $2 \cdot N_f$ . The experimental points were fitted by Basquin's law

$$\sigma_a = \sigma_f' (2N_f)^b \quad (4.1)$$

where  $\sigma_f'$  stands for fatigue strength coefficient and  $b$  for fatigue strength exponent. The values were evaluated by regression analysis using the least squares approach and are listed in Table 4. The plot clearly shows that in a service-relevant stress cycling, the aged material performs markedly better. In strain cycling, however, the solutionised material achieves higher lifetimes which is connected to lower stress levels. Fig. 4.1b shows a plot of half-life plastic strain amplitude  $\varepsilon_{ap,50\%N_f}$  vs. double lifetime  $2 \cdot N_f$ . The experimental points were fitted by Coffin-Manson's law

$$\varepsilon_{ap} = \varepsilon_f' (2N_f)^c \quad (4.2)$$

where  $\varepsilon_f'$  stands for fatigue ductility coefficient and  $c$  for fatigue ductility exponent. The values were evaluated by regression analysis using the least squares approach and are listed in Table 4. As follows from the plot, the solutionised material attains higher levels of plastic strain amplitude at half-life. The difference in attained plasticity at half-life becomes bigger at lower imposed strains. It is illustrated by different slopes of the fitting curves. Flow stress is higher for the aged material as shown by cyclic stress-strain curves in the representation of half-life stress amplitude  $\sigma_{a,50\%N_f}$  vs. half-life plastic strain amplitude  $\varepsilon_{ap,50\%N_f}$ , shown in Fig. 4.1c. The experimental points in the plot were fitted by a power law in the form

$$\sigma_a = K \varepsilon_{ap}^n \quad (4.3)$$

where  $K$  is an experimentally determined material constant and  $n$  stands for cyclic strain hardening exponent. The values were evaluated by regression analysis using the least squares approach and are listed in Table 4.

In both thermodynamical states, room temperature damage was fatigue-dominated, as documented in Fig. 4.2a–c for the solutionised and in Fig. 4.2d–f for the aged material. Fracture surfaces exhibited multiple crack initiation, and contained striations and/or dimples, indicating transgranular fatigue crack propagation, which is typical for superalloys tested at room temperature [11]. The inspection of polished specimen surfaces revealed extensive roughening by PSMs with numerous cracks along them (Fig. 4.2c,f), in agreement with previous investigations on superalloys [9, 11, 17]. Clearly, PSMs were key to fatigue crack initiation which is further supported by the statistics on the occurrence of secondary cracks shown in Fig. 4.3. Since the occurrence of PSMs is a manifestation of cyclic plastic straining of the material, it can be concluded that the room-temperature fatigue lifetime of René 41 superalloy in both solutionised and aged states is governed by plastic strain amplitude.

### 4.1.2 High temperature (800 °C) fatigue loading

At 800 °C, it makes sense to investigate only the aged material since the ageing temperature for René 41 is 760 °C. In comparison to the aged material subjected to room temperature fatigue, cyclic stresses are reduced (see Fig. 4.1a). The performance deteriorates in both stress (Fig. 4.1a shows that the 800 °C curve lies generally below) and strain cycling (Fig. 4.1b). For instance, comparing the aged specimens cycled with  $\varepsilon_a = 0.8\%$ , the lifetime decreased tenfold. This is further complemented by lowering the flow stress (see Fig. 4.1c). The diagram in Fig. 4.1b shows there is also a significant drop in the number of cycles to failure at a given plastic strain amplitude.

The fracture surfaces were predominantly intergranular (Fig. 4.4a–b), which is indicative of a damaging mechanism other than fatigue. Intergranular cracking has been widely reported in superalloys subjected to fatigue at high temperatures [10–11, 17]. Fig. 4.4c–e show the specimen surface covered by a non-uniform oxidic layer (see Fig. 4.4e) with roughly the same composition as observed by Jiang *et al.* [18]. The oxide layer appeared thicker at grain boundaries and at other weak points of the microstructure, such as twin boundaries and PSMs (Fig. 4.4c). Extensive subsurface damage (Fig. 4.4d) occurred mostly along the grain boundaries, where the oxides formed in voids along the grain boundaries, and at the newly formed microcracks' surfaces. Since the extent of subsurface oxidation (10–15  $\mu\text{m}$  at  $\varepsilon_a = 0.5\%$ ) is significantly higher than predicted by load-free stability tests [14], it can be assumed that cyclic stresses accelerated the penetration of oxygen. This altogether indicates an interaction of fatigue (cyclic plasticity via persistent slip bands (PSBs)/PSMs on the surface, Fig. 4.4c), environmental (surface oxidation, Fig. 4.4c) and creep (voids along the grain boundaries in Fig. 4.4d) damage. Since the cracking of the oxidised grain boundaries is prevalent (see Fig. 4.3), it can be concluded that the low-cycle fatigue lifetime of René 41 superalloy at 800 °C is determined by the extent of environmental attack.

Since vast majority of secondary cracks was found to initiate from the grain boundaries (Fig. 4.3), it is clear that the principal acting mechanism is grain boundary oxidation, in agreement with other studies on superalloys [10, 17–18]. Cracking along twin boundaries and slip bands (producing PSMs) occurs too, however, grain boundary cracking is more favourable due to the easy diffusion of oxygen along them. The diffusion of oxygen along the grain boundaries, resulting in internal oxide formation [19], is promoted by high stresses [20] and positively influenced by temperature concerning Arrhenius-type dependence. The source of elements for internal oxide formation can be the surrounding matrix (primarily a source of Cr [21], which is getting depleted as shown in Fig. 4.4e), and secondary phases (e.g., TiC might provide Ti for internal Ti oxides [22]).

Table 4. Fitting curves coefficients and exponents.

René 41	$\sigma_f'$ (MPa)	b (-)	$\varepsilon_f'$ (%)	c (-)	K (MPa/100)	n (-)
Solutionised, fatigue at RT	1872	-0.073	82.15	-0.603	874.1	0.127
Aged, fatigue at RT	1568	-0.079	577.8	-0.884	1109	0.081
Aged, fatigue at 800 °C	2021	-0.135	58.34	-0.835	1041	0.161

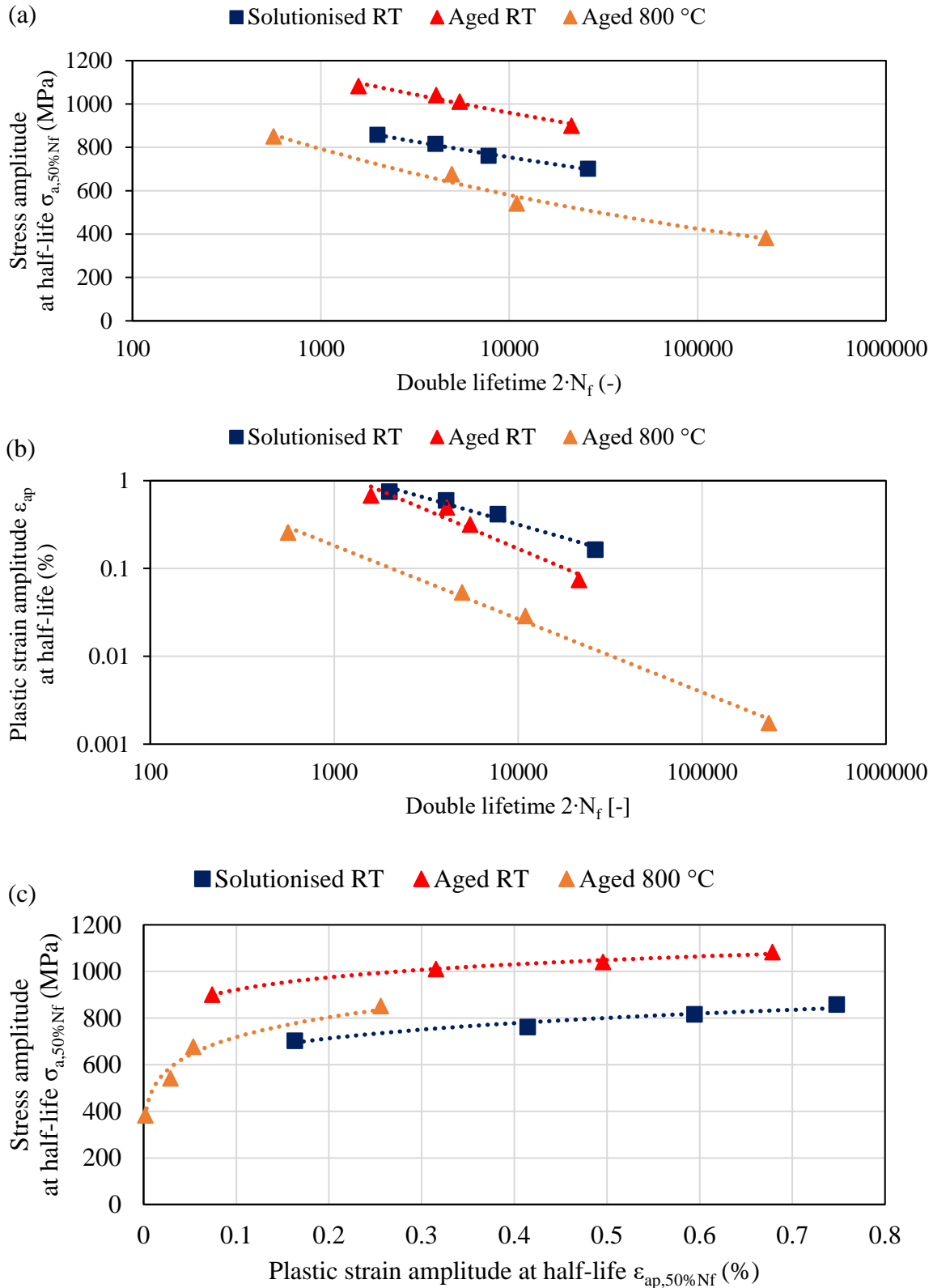


Fig. 4.1. Analyses of fatigue performance of René 41 superalloy, cycled at RT and 800 °C. (a) Basquin and (b) Coffin-Manson lifetime representation. (c) Cyclic stress-strain curve in the representation of half-life stress amplitude  $\sigma_{a,50\%N_f}$  vs. half-life plastic strain amplitude  $\varepsilon_{ap,50\%N_f}$ .

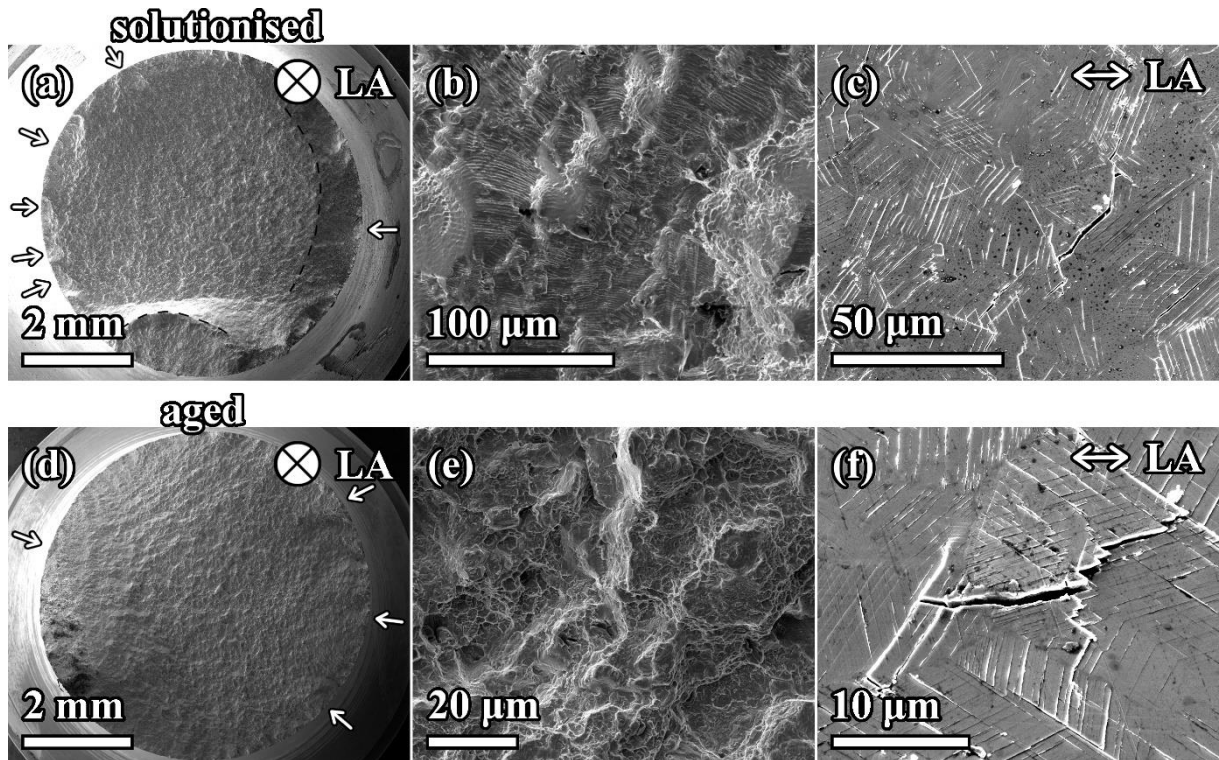


Fig. 4.2. SEM micrographs showing fatigue damage imposed on (a–c) solutionised René 41 superalloy cycled with  $\varepsilon_a = 0.5\%$  at RT, observed *post-mortem*. (a) Overview of fracture surface with multiple fatigue crack initiation (pointed out by arrows) and highlighted areas of fatigue crack growth, (b) a detail showing a crack initiation site with striations corresponding to early crack propagation. (c) Specimen surface relief with extensive PSM formation and secondary cracks along the PSMs. (d–f) Fatigue damage imposed on aged René 41 superalloy cycled with  $\varepsilon_a = 0.8\%$  at RT, observed *post-mortem*. (d) Overview of fracture surface with multiple fatigue crack initiation (pointed out by arrows), (e) transgranular dimple-like character of fracture surface in detail. (f) Detail showing secondary cracks along the PSMs.

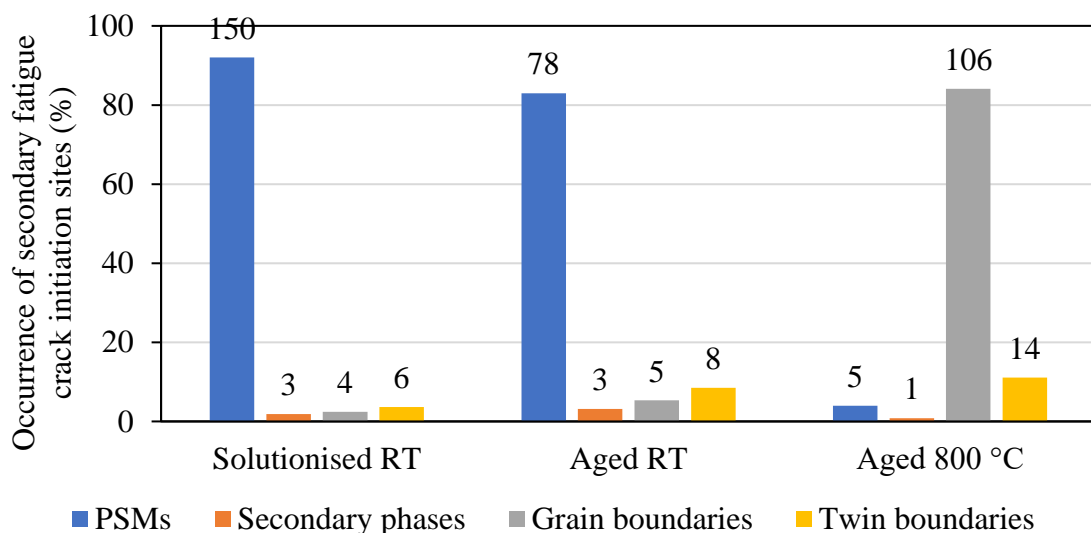


Fig. 4.3. Chart depicting a shift of initiation sites of secondary fatigue cracks in René 41 superalloy cycled with  $\varepsilon_a = 0.5\%$  from predominant PSMs at room temperature (RT) to other initiation sites at 800 °C, particularly to the grain boundaries. The number of corresponding sites is labelled above the respective bars. Note that the initiation sites were evaluated over a distance of 2 mm from the fracture surface.

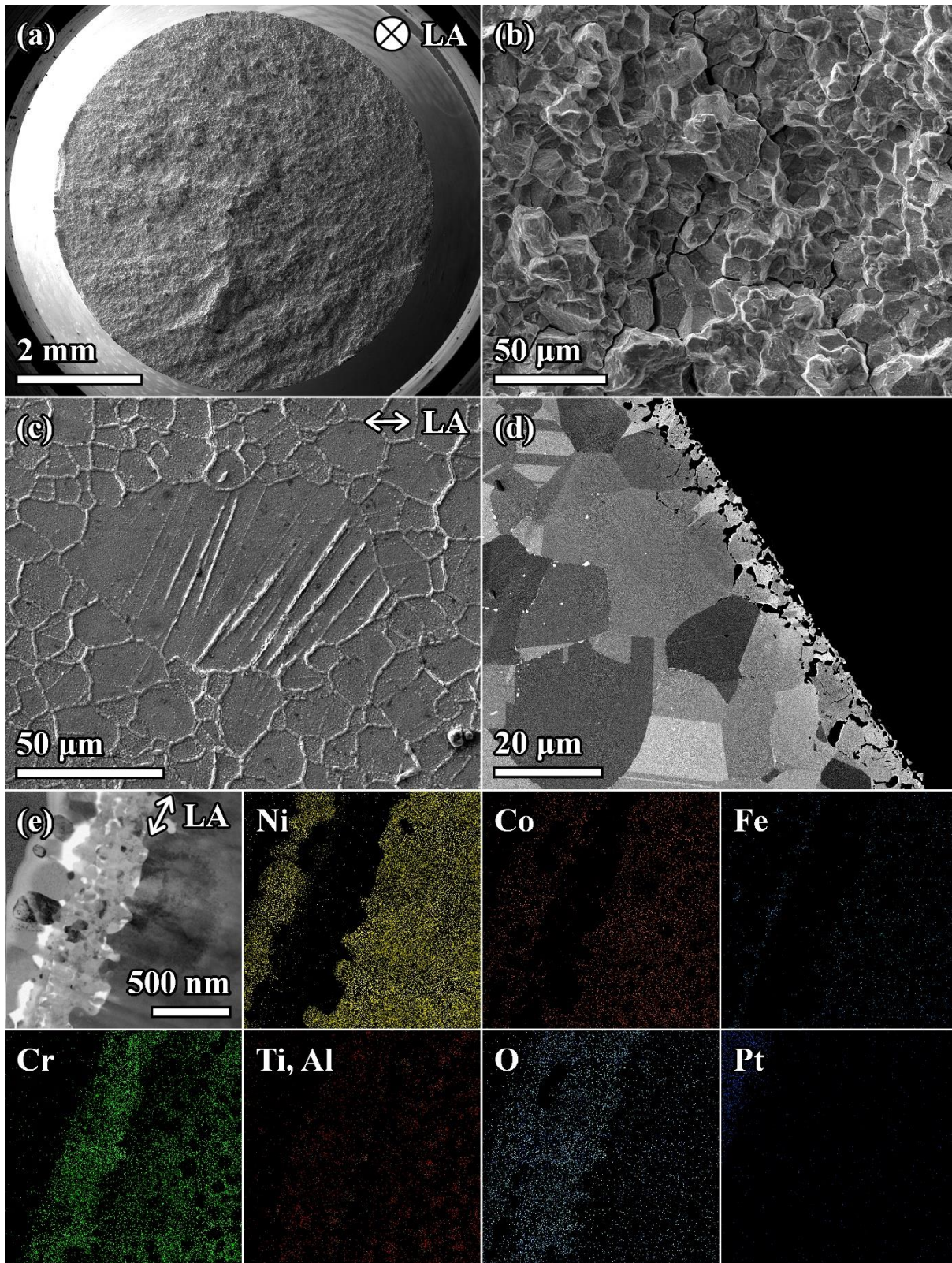


Fig. 4.4. Analysis of overall damage imposed on aged René 41 superalloy cycled with  $\epsilon_a = 0.5\%$  at  $800\text{ }^\circ\text{C}$ , observed *post-mortem*. (a–d) SEM micrographs of (a) a fracture surface with (b) a detail showing intergranular fracture with numerous facets corresponding to crack propagation along the grain boundaries, (c) oxidised specimen surface with preferential oxidation at grain boundaries, twin boundaries, and slip markings, and (d) cross-section showing the extent of subsurface damage. (e) STEM+EDS analysis reveals the composition of the oxidic layer on top of a grain.

## 4.2 Analysis of cyclic deformation behaviour

### 4.2.1 Room temperature fatigue loading

Fig. 4.6 shows cyclic hardening/softening curves in representations of stress amplitude  $\sigma_a$  and plastic strain amplitude  $\varepsilon_{ap}$  vs. the number of cycles  $N$ . Generally, saturation plateau was absent in the range of tested strain amplitudes. The evolution of cyclic stresses of solutionised René 41 superalloy is typical behaviour for room-temperature fatigue of  $\gamma'$ -free superalloys such as solid solution-strengthened superalloy Hastelloy-X [23]. There was an initial rapid cyclic hardening manifested by the gradual increase of stress amplitude and a decrease in plastic strain amplitude. Cyclic hardening can be attributed to high strains promoting dislocation multiplication and dislocation interactions occurring in both matrix and the newly formed slip bands. Unlike Hastelloy-X [23], solutionised René 41 tends not to saturate the cyclic response but rather evolve into cyclic softening. This can be ascribed to the localization of cyclic slip into the intensive PSBs (see Fig. 4.8), which becomes increasingly dominant.

The analysis of the hysteresis loop using the statistical approach (Fig. 4.7a) [16] showed that solutionised René 41 exhibited a single major peak in the second derivative. This corresponds well with the microstructure exhibiting only one phase being deformed. The evolution of the peak corresponds to the observed cyclic behaviour, as the peak first shifts towards higher fictive stresses (cyclic hardening), but eventually shifts back towards lower stresses (cyclic softening).

Aged René 41 (Fig. 4.6b) exhibits no or negligible cyclic hardening (maximum increase in  $\sigma_a$  is 30 MPa for  $\varepsilon_a = 1.2\%$  which constitutes a 2.5% increase), the dominant feature is gradual cyclic softening until fracture. In comparison with the solutionised state, cyclic stresses attained by the aged material are higher due to the dispersion of  $\gamma'$  precipitates, which represent a principal obstacle to dislocation movement and thus increase the flow stress (Fig. 4.1c). Cyclic deformation behaviour is similar to other wrought Ni-based superalloys such as Waspaloy [9]. The initial hardening stage is rather short and is followed by softening stage which later evolve almost into stress saturation. This is indicative of synergistic mechanisms contributing to cyclic softening in the early stages of fatigue life, presumably cyclic slip localization into PSBs and shearing of the coherent  $\gamma'$ . A stronger cyclic softening in the early stages of the fatigue life hints that shearing of  $\gamma'$  apparently plays a significant role only in this period.

The experimental curve of the second derivative (Fig. 4.7b) of aged René 41 cycled with  $\varepsilon_a = 0.8\%$  exhibits two separate peaks, which corresponds to the deformation of two phases in multiphase material [24]. In the present work, the peaks are attributed to the  $\gamma$  matrix and the  $\gamma'$  precipitates, which both can be sheared by moving dislocations. While the first peak (at lower fictive stresses, attributed thus to the matrix) gradually grows and shifts towards lower fictive stresses, the second peak (at higher stresses, attributed thus to the  $\gamma'$  precipitates) vanishes completely in less than 10 cycles. The evolution of the first peak is indicative of softening of the matrix, which is well in agreement with observations on cyclic slip localization into PSBs (see Fig. 4.8). The evolution of the second peak witnesses a substantial decrease in the number of deformed microvolumes with high fictive stress. This indicates that  $\gamma'$  precipitates are sheared in larger numbers only in the first few cycles. Early shearing of the  $\gamma'$  observed in this study is shown in Fig. 4.9f. The result also indicates that later on, deformation is mostly confined to the matrix, and only the underaged or previously sheared precipitates with lower flow stress are deformed too. It can thus be assumed that the majority of slip bands is formed at the beginning of the fatigue life, slip is confined to them, they shear the precipitates, and slip within the slip bands intensifies over the fatigue life. This agrees with a detailed study on the cyclic slip in Ni-based superalloys by Mello *et al.* [25]. The precipitates that interfere with slip bands are continuously sheared until they impart almost no resistance to further dislocation

movement, hence the second peak diminishes. Shearing of the  $\gamma'$  precipitates is often considered an important mechanism contributing to the observed softening behaviour [9]. However, as follows from the analysis of the hysteresis loops, this does not seem to be the case for René 41 superalloy, which witnesses considerable shearing of the  $\gamma'$  only in the first few cycles. This result suggests that in the fatigue-related material design of superalloys, a higher focus should be paid to the strengthening of the matrix.

#### 4.2.2 High temperature (800 °C) fatigue loading

The character of the overall cyclic stress response over cycling is for aged René 41 similar for elevated and room temperatures, although cyclic stresses are notably lower (e.g., by about 300 MPa for  $\varepsilon_a = 0.5\%$ ; Fig. 4.6b–c). This is related to lower elastic modulus and flow stress at high temperatures as indicated by cyclic stress-strain curves shown in Fig. 4.1c. Although cyclic stress response (see Fig. 4.6c) is rather stable at low strain amplitudes, there is a tendency to cyclic softening with increasing strain amplitude, which can be related to plastic straining induced by high cyclic stresses. Similar behaviour is exhibited by only a few other wrought superalloys such as René 77 [26]. Softening is promoted by localization of cyclic slip in PSBs and by shearing of  $\gamma'$  precipitates, in agreement with other studies on high-temperature deformation of Ni-based superalloys [10–11, 17].

In comparison to the room temperature, deformation at 800 °C is more homogeneous, which is manifested in frequent shearing of  $\gamma'$  precipitates (Fig. 4.5a) and a lower tendency to form slip bands (Fig. 4.5b). Analysis of the loop shape using the statistical theory of the hysteresis loop was performed on a specimen cycled with  $\varepsilon_a = 0.8\%$  (Fig. 4.7c). From the first cycle throughout the fatigue life, two major peaks in the second derivative occurred. This contrasts with fatigue loading at RT, which witnessed a swift vanishing of the second peak occurring at higher fictive stress. The occurrence of the two peaks indicates the deformation of the two dominant phases in René 41 superalloy, namely the  $\gamma$  matrix and the  $\gamma'$  precipitates. The first peak at about 600 MPa (corresponding to  $\gamma$ ) in the first cycle gradually shifted towards lower fictive stress (cyclic softening), and the peak became increasingly pronounced, which indicates that the deformation of the matrix is intensifying throughout the fatigue life. This can be attributed to the cyclic slip in PSBs, which shear away the precipitates standing in the way, until they offer no resistance to the cyclic slip. The second peak was dominant in the first cycle, but gradually decreased so that its height was in the end lower than that of the first peak. This suggests that shearing of  $\gamma'$  was taking place throughout the fatigue life, however, its significance gradually decreased.

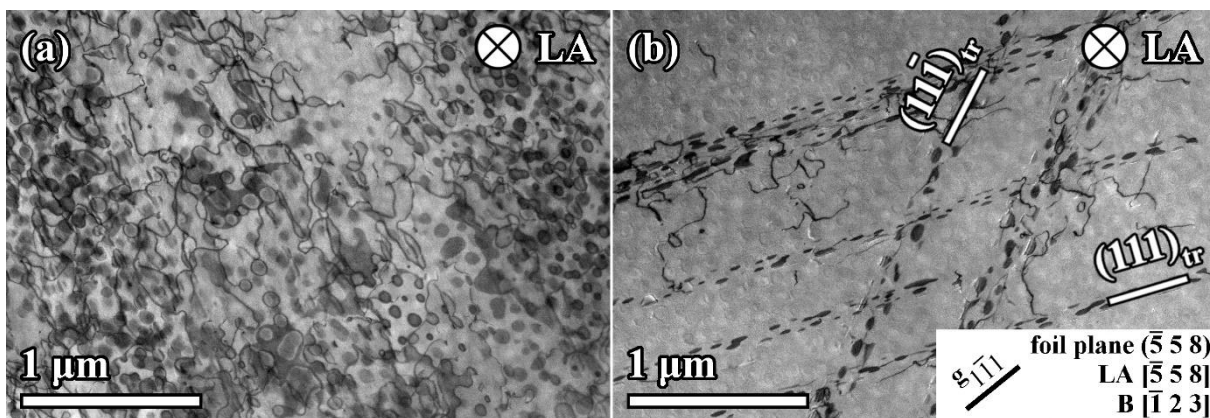


Fig. 4.5. STEM micrographs of aged René 41 cycled with  $\varepsilon_a = 0.5\%$  at 800 °C, observed *post-mortem*. (a) A grain deformed rather homogeneously, no traces of slip bands were observed. (b) Slip bands having sheared the  $\gamma'$ , leaving stacking faults behind.

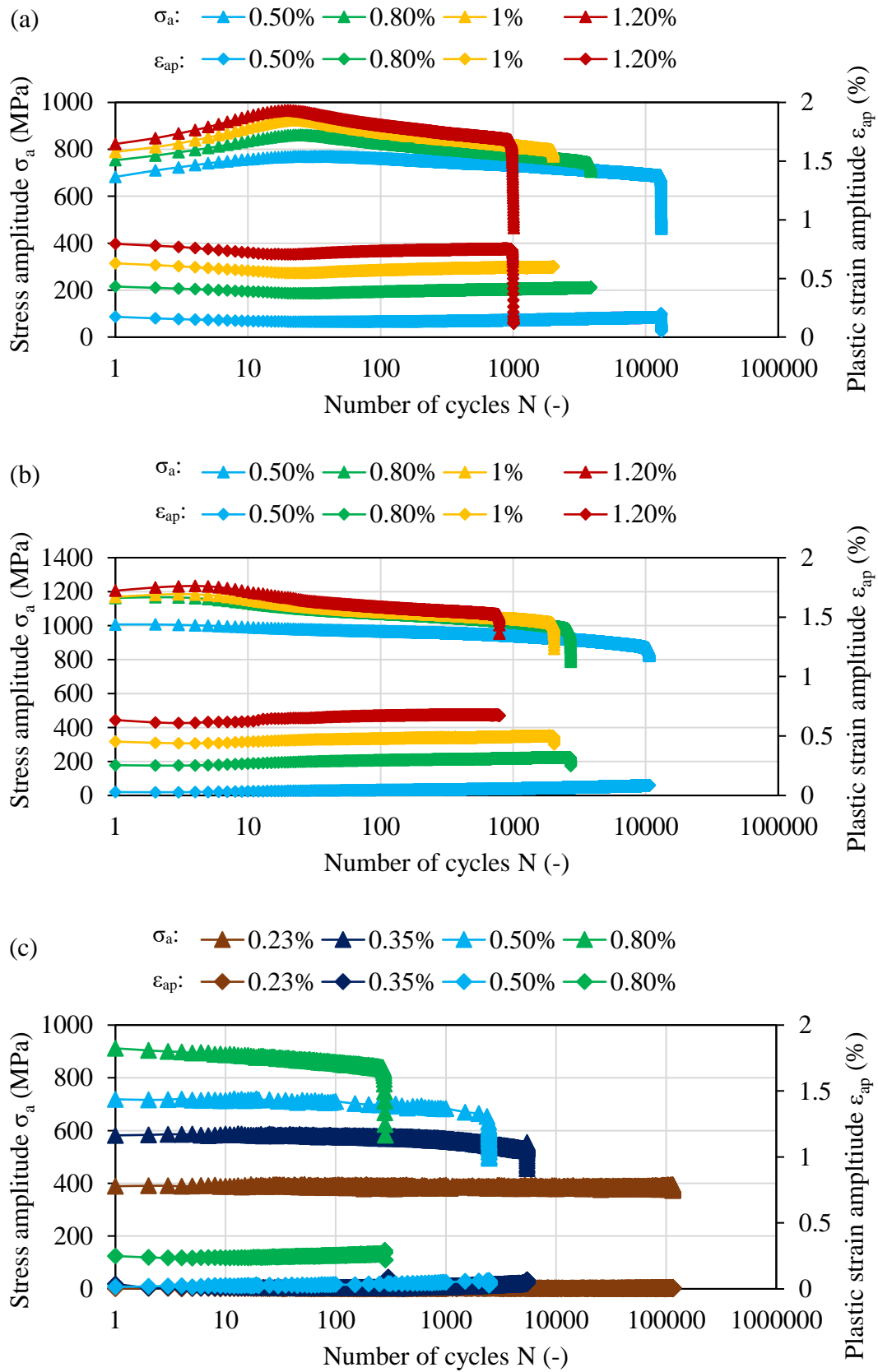


Fig. 4.6. Cyclic hardening/softening curves of René 41 superalloy cycled at RT and 800 °C. (a) Solutionised René 41 at RT. (b) Aged René 41 at RT. (c) Aged René 41 at 800 °C.

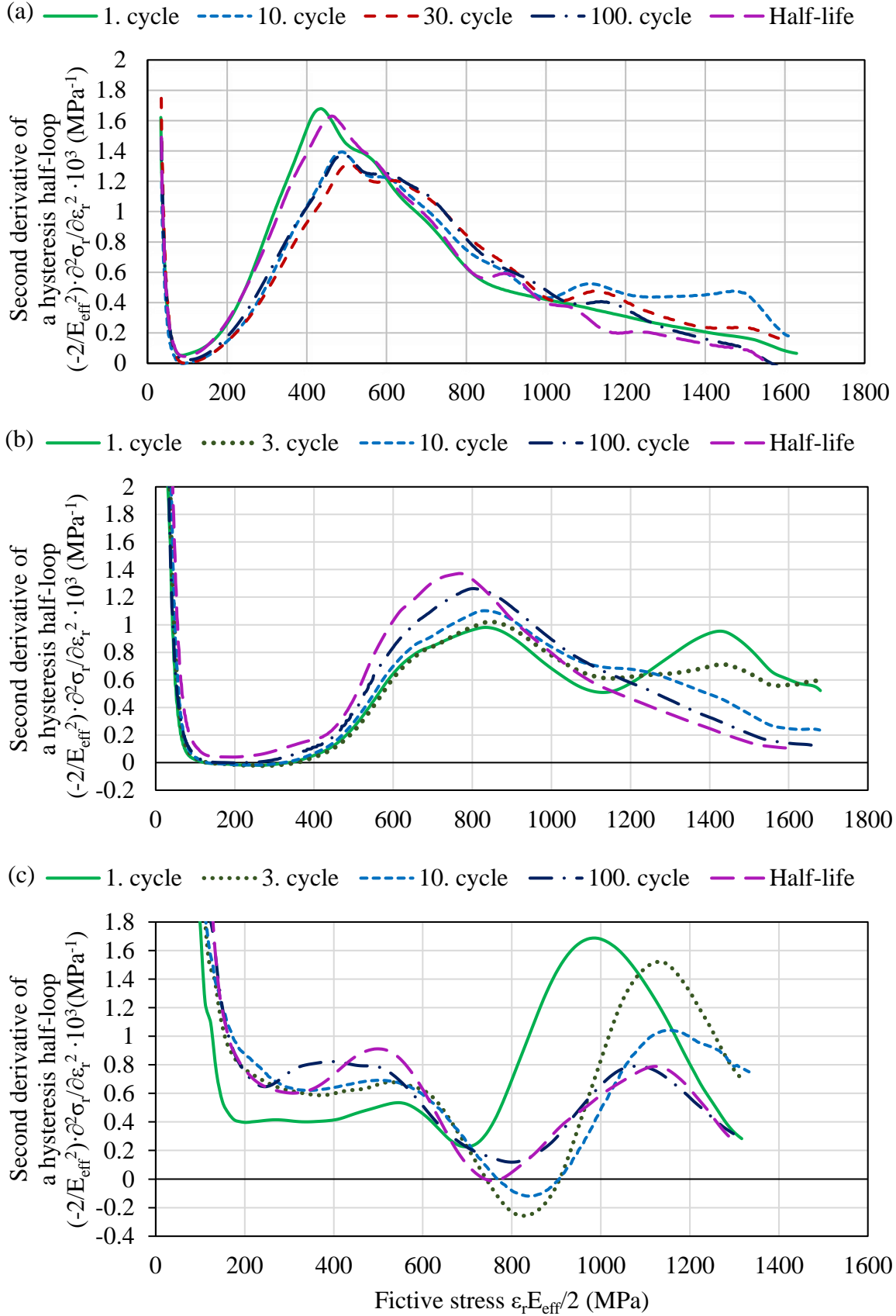


Fig. 4.7. Evolution of the second derivative of the compressive half-loop for (a) solutionised René 41 cycled at RT, (b) aged René 41 cycled at RT and (c) aged René 41 cycled at 800 °C.

### 4.3 Evolution of surface relief and the underlying microstructure

The evolution of features occurring on the surface due to cyclic slip was thoroughly studied on specimens cycled with  $\varepsilon_a = 0.8\%$  at room temperature. The testing was interrupted after a definite number of cycles and the resulting surface roughening and dislocation structures were studied. The interruptions were performed following the procedure described in Chapter 3.2.3. On a qualitative basis, surface features developed in a same manner in solutionised and aged state, with only difference being the presence of shearable  $\gamma'$  precipitates in the latter.

STEM inspection (Fig. 4.8a and Fig. 4.9a–d) of lamellae extracted from the specimen surface after one cycle revealed thin planar dislocation arrays on  $\{111\}$  planes, parallel to the trace of primary slip plane – slip bands. This proves that cyclic slip is localized into PSBs since the first cycle, consistently with other Ni-based superalloys [25, 27]. The arrangement in slip bands was in several cases linked with the formation of sharp-edged slip steps on the surface, which occasionally formed material extrusions (Fig. 4.9d). The occurrence of slip steps corresponds well to the predictions based on random slip events in PSBs by Differt *et al.* [6]. Shape and character of slip steps was studied in an appreciable detail by Stinville *et al.* [27].

More complex slip markings consisting of a shallow elevation (extrusion) and a deepening parallel (intrusion) to it were identified after 10 cycles (see Fig. 4.8b and Fig. 4.9e). The slip markings emerged on the surface because of the repeated strain localisation in the slip bands. Due to the nature of the bands, in which cyclic slip had already been concentrated for a considerable number of cycles, the slip bands were identified as persistent slip bands (PSBs) and the corresponding relief atop the PSBs as persistent slip markings (PSMs). Due to the planar character of slip, the PSBs do not assume ladder-like structure like in simple metals [4–5].

With continued fatigue loading, slip in PSBs intensified, and the resulting PSMs were becoming more complex in shape. This can be explained by diffusion effects becoming prevalent later in the fatigue life [28], redistributing matter across PSB/matrix interface [4–5]. The PSBs were often grouped into more complex planar arrays (macro-PSBs) consisting of several individual bands as indicated in Fig. 4.8c. The identification of individual PSBs was at this point already impossible. The resulting macro-PSMs were complex in shape, usually formed by alternating extrusions and intrusions and thus reflecting the strain history of several parallel PSBs at once. Two types of intrusions were identified: (i) sharp thin intrusions, closely accompanying extrusions (Fig. 4.8e), and (ii) rather shallow and wide intrusions (Fig. 4.8c) with sharp edges, indicating the formation by a series of slip steps. Thin intrusions were causing a considerable notch effect, and were usually found on one side of a macro-PSM (at a PSB/matrix interface), but in some cases they occurred on both sides or in the midst of a PSM.

With an increasing number of elapsed cycles, unanimous microcracks formed. E.g., Fig. 4.8f shows a microcrack originating from a PSM at the surface and propagating along the slip plane after 500 cycles. At this point, the surface was decorated by densely distributed, complex-shaped macro-PSMs with thin parallel intrusions, and abundant microcracks which developed from them. It is unclear at which point an intrusion becomes a microcrack, and even whether the intrusion is an actual microcrack as reasoned by Mughrabi [29] based on the EGM model [5]. It can be argued that some of the assumptions by the EGM model are incorrect since the predicted height and shape vary significantly from the observations conducted in this work (for more details see the full version of the thesis). The shapes of the observed PSMs correspond better to Polák's model [4] predicting extrusion growth with parallel intrusions occurring later the side of an extrusion. However, quantification of the surface features using the Polák's approach has not been a part of this study, hence Polák's model could not be verified for René 41 superalloy.

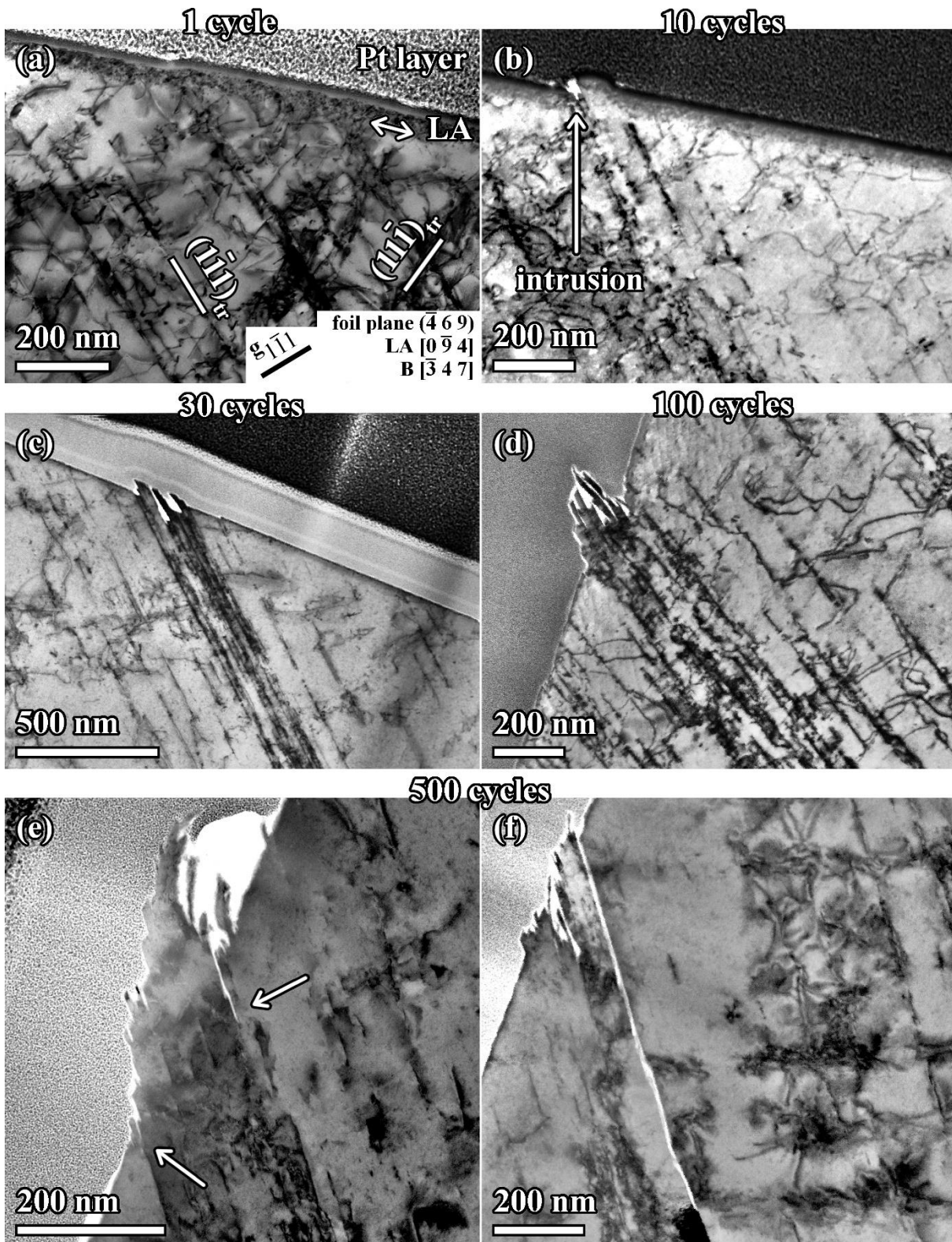


Fig. 4.8. STEM micrographs of solutionised René 41 superalloy cycled with  $\varepsilon_a = 0.8\%$  at RT, showing the evolution of surface relief and the underlying dislocation arrangements after (a) 1 cycle, (b) 10 cycles, (c) 30 cycles, (d) 100 cycles and (e–f) after 500 cycles also with microcracks. The cross-sections are parallel to the loading axis (LA). Reproduced from [30].

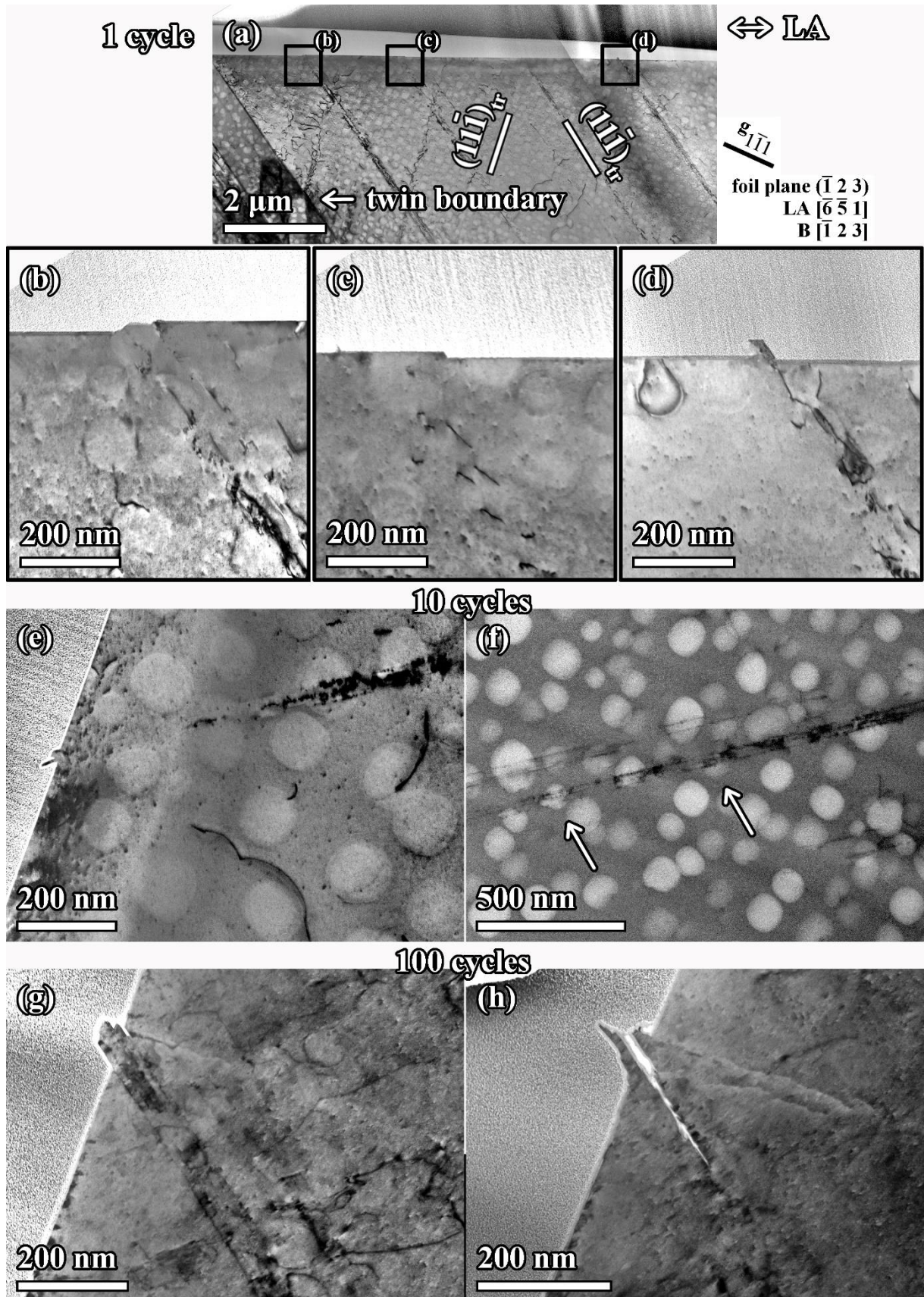


Fig. 4.9. STEM micrographs of aged René 41 superalloy cycled with  $\varepsilon_a = 0.8\%$  at RT, showing the evolution of surface relief and the underlying dislocation arrangements after (a–d) 1 cycle, (e–f) 10 cycles and (g–h) 100 cycles also with microcracks. The cross-sections are parallel to the loading axis (LA). Reproduced from [30].

## 5 Conclusions

In the present work, fatigue tests were conducted on René 41 superalloy in a low-cycle fatigue regime at room and elevated (800 °C) temperatures. The resulting stress-strain response was analysed using the statistical theory of the hysteresis loop to identify the character of cyclic deformation over fatigue life. Fatigue data were related to microscopy observations taken by scanning and transmission electron microscope. The general conclusions are as follows:

Regarding the lifetime and damage behaviour of the investigated alloy, the following conclusions can be drawn:

- At room temperature, the damage is mostly transgranular, and the lifetime is governed by plastic strain amplitude. This is due to fatigue cracks initiating predominantly from persistent slip markings created on the surface as a consequence of the localization of cyclic plastic strain in persistent slip bands.
- Exposure to fatigue at 800 °C results in significantly shorter lifetimes due to environmental damage in the form of oxides on the surface. The resulting damage is mostly intergranular due to relatively low material integrity at the grain boundaries, which is reduced by oxygen diffusion and carbide coarsening.

Regarding the deformation behaviour, the following conclusions can be drawn:

- At room temperature, plastic deformation is highly inhomogeneous. Two major competing mechanisms were recognized: initial increase in dislocation density promoting cyclic hardening, and localization of cyclic slip in persistent slip bands promoting softening behaviour. Softening by shearing of coherent  $\gamma'$  precipitates is significant only in the early stages of fatigue life, which might be enough to counter the initial cyclic hardening.
- At 800 °C, plastic deformation is more homogeneous. Localization of cyclic slip is less pronounced and the  $\gamma'$  shearing is abundant, although decreasingly occurrent over fatigue life. Both mechanisms contribute to cyclic softening. Slip bands were observed exclusively along octahedral crystallographic planes.

From the detailed study on the localization of cyclic slip and consequent formation of surface relief over fatigue life of René 41 superalloy, published previously in [30], the following conclusions can be drawn:

- Cyclic slip is localized to persistent slip bands from the first cycle. Consequently, surface roughening arises in the form of persistent slip markings that consist of slip steps, extrusions and intrusions.
- The majority of persistent slip bands nucleates very early in the fatigue life.
- Later in fatigue life, vacancies are produced due to dislocation interactions and diffusion effects become significant. A more complex relief in the form of extrusions and intrusions arises. Intrusions are sharp, generally appear later, and cause a significant notch effect for fatigue crack initiation.
- The shape of the persistent slip markings is predicted well by the EGM model [5] as well as Polák's model [4]. However, the former yields a notable discrepancy between predicted and observed extrusion heights. This, together with resistivity measurements [28], implies an underestimation of the diffusion effects in favour of Polák's model. Nevertheless, Polák's model could not be verified in the present research due to missing data for the quantification of surface features. Hence, further effort in this direction should be made in future.

## 6 References

- [1] POLÁK, J. *Cyclic Plasticity and Low Cycle Fatigue Life of Metals*. 2nd ed. Prague: Academia, 1991. ISBN 8020000089.
- [2] ABEL, A. Fatigue of copper single crystals at low constant plastic strain amplitudes. *Materials Science and Engineering*. 1978, **36**(1), 117–124. ISSN 0025-5416. DOI:10.1016/0025-5416(78)90201-X
- [3] BROOM, T. and R. HAM. The hardening of copper single crystals by fatigue. *Proceedings of the Royal Society of London. Series A. Mathematical and Physical Sciences*. 1959, **251**(1265), 186–199. ISSN 0080-4630. DOI:10.1098/rspa.1959.0101
- [4] POLÁK, J. On the role of point defects in fatigue crack initiation. *Materials Science and Engineering*. 1987, **92**, 71–80. ISSN 0025-5416. DOI:10.1016/0025-5416(87)90157-1
- [5] ESSMANN, U., U. GÖSELE and H. MUGHRABI. A model of extrusions and intrusions in fatigued metals I. Point-defect production and the growth of extrusions. *Philosophical Magazine A*. 1981, **44**(2), 405-426. ISSN 0141-8610. DOI:10.1080/01418618108239541
- [6] DIFFERT, K., U. ESMANN and H. MUGHRABI. A model of extrusions and intrusions in fatigued metals II. Surface roughening by random irreversible slip. *Philosophical Magazine A*. 1986, **54**(2), 237-258. ISSN 0141-8610. DOI:10.1080/01418618608242897
- [7] REPETTO, E. and M. ORTIZ. A micromechanical model of cyclic deformation and fatigue-crack nucleation in f.c.c. single crystals. *Acta Materialia*. 1997, **45**(6), 2577-2595. ISSN 1359-6454. DOI:10.1016/S1359-6454(96)00368-0
- [8] PINEAU, A. and S. ANTOLOVICH. High temperature fatigue of nickel-base superalloys - A review with special emphasis on deformation modes and oxidation. *Engineering Failure Analysis*. 2009, **16**(8), 2668–2697. ISSN 1350-6307. DOI:10.1016/j.engfailanal.2009.01.010
- [9] MERRICK, H.F. The low cycle fatigue of three wrought nickel-base alloys. *Metallurgical Transactions*. 1974, **5**(4), 891-897. ISSN 0360-2133. DOI:10.1007/BF02643144
- [10] LERCH, B., N. JAYARAMAN and S. ANTOLOVICH. A study of fatigue damage mechanisms in Waspaloy from 25 to 800°C. *Materials Science and Engineering*. 1984, **66**(2), 151-166. ISSN 0025-5416. DOI:10.1016/0025-5416(84)90177-0
- [11] ANTOLOVICH, S.D. and B. LERCH. Cyclic Deformation, Fatigue and Fatigue Crack Propagation in Ni-base Alloys. In: *Superalloys, Supercomposites, Superceramics*. Elsevier, 1989, s. 363-411. ISBN 9780126908459. DOI:10.1016/B978-0-12-690845-9.50018-X
- [12] PHILLIPS, E.P. *Fatigue of René 41 Under Constant- and Random- Amplitude Loading at Room and Elevated Temperatures*. Washington, D.C.: National Aeronautics and Space Administration, 1965. NASA TN D-3075.
- [13] ELKIND, S. A radiation-cooled nuclear rocket nozzle for long firing durations. *Journal of Spacecraft and Rockets*. 1965, **2**(3), 353-357. ISSN 0022-4650. DOI:10.2514/3.28183
- [14] DONACHIE, M. and S. DONACHIE. *Superalloys. A Technical Guide*. 2nd ed. Materials Park: ASM International, 2002. ISBN 0871707497.
- [15] KAYACAN, R., R. VAROL and O. KIMILLI. The effects of pre- and post-weld heat treatment variables on the strain-age cracking in welded Rene 41 components. *Materials Research Bulletin*. 2004, **39**(14-15), 2171-2186. ISSN 0025-5408. DOI:10.1016/j.materresbull.2004.08.003
- [16] POLÁK, J. and M. KLESNIL. The Hysteresis Loop 1. A Statistical Theory. *Fatigue of Engineering Materials and Structures*. 1982, **5**(1), 19–32. ISSN 0160–4112. DOI:doi.org/10.1111/j.1460-2695.1982.tb01221.x
- [17] ŠULÁK, I. and K. OBRTLÍK. AFM, SEM and TEM study of damage mechanisms in cyclically strained MAR-M247 at room temperature and high temperatures. *Theoretical and Applied Fracture Mechanics*. 2020, **108**. ISSN 0167-8442. DOI:10.1016/j.tafmec.2020.102606

- [18] JIANG, R., D. PROPRENTNER, M. CALLISTI, B. SHOLLOCK, X.T. HU, Y.D. SONG and P.A.S. REED. Role of oxygen in enhanced fatigue cracking in a PM Ni-based superalloy: Stress assisted grain boundary oxidation or dynamic embrittlement?. *Corrosion Science*. 2018, **139**, 141-154. ISSN 0010-938X. DOI:10.1016/j.corsci.2018.05.001
- [19] YANG, S., U. KRUPP, H.-J. CHRIST and V. BRAZ TRINDADE. The Relationship between Grain Boundary Character and the Intergranular Oxide Distribution in IN718 Superalloy. *Advanced Engineering Materials*. 2005, **7**(8), 723-726. ISSN 1438-1656. DOI:10.1002/adem.200500036
- [20] WAGENHUBER, E.-G., V.B. TRINDADE and U. KRUPP. The Role of Oxygen-Grain-Boundary Diffusion During Intercrystalline Oxidation and Intergranular Fatigue Crack Propagation in Alloy 718. In: *Superalloys 718, 625, 706 and Various Derivatives (2005)*. TMS, 2005, s. 591-600. ISBN 9780873396028. DOI:10.7449/2005/Superalloys\_2005\_591\_600
- [21] ROMAIN, C., D. TEXIER, C. DESGRANGES, J. CORMIER, S. KNITTEL, D. MONCEAU and D. DELAGNES. Oxidation of Thin Nickel-Based Superalloy Specimens: Kinetics Study and Mechanical Integrity. *Oxidation of Metals*. 2021, **96**(1-2), 169-182. ISSN 0030-770X. DOI:10.1007/s11085-021-10075-2
- [22] LYTLE, F.W., R.B. GREGOR and T. LUHMAN. Examination of the titanium environment in a René 41 nickel base superalloy by X-ray absorption spectroscopy. *Metallurgical Transactions A*. 1986, **17**(4), 739-741. ISSN 0360-2133. DOI:10.1007/BF02643995
- [23] JABLONSKI, D.A. *Fatigue Behavior of Hastelloy X at Elevated Temperatures in Air, Vacuum and Oxygen Environment*. 1978. Dissertation thesis. Massachusetts Institute of Technology. Vedoucí práce R.M. Pelloux.
- [24] POLÁK, J., F. FARDOUN and S. DEGALLAIX. Analysis of the hysteresis loop in stainless steels II. Austenitic–ferritic duplex steel and the effect of nitrogen. *Materials Science and Engineering: A*. 2001, **297**(1-2), 154-161. ISSN 0921-5093. DOI:10.1016/S0921-5093(00)01252-1
- [25] MELLO, A.W., A. NICOLAS and M.D. SANGID. Fatigue strain mapping via digital image correlation for Ni-based superalloys: The role of thermal activation on cube slip. *Materials Science and Engineering: A*. 2017, **695**, 332-341. ISSN 0921-5093. DOI:10.1016/j.msea.2017.04.002
- [26] ANTOLOVICH, S.D., E. ROSA and A. PINEAU. Low cycle fatigue of René 77 at elevated temperatures. *Materials Science and Engineering*. 1981, **47**(1), 47-57. ISSN 0025-5416. DOI:10.1016/0025-5416(81)90040-9
- [27] STINVILLE, J.C., P.G. CALLAHAN, M.A. CHARPAGNE, M.P. ECHLIN, V. VALLE and T.M. POLLOCK. Direct measurements of slip irreversibility in a nickel-based superalloy using high resolution digital image correlation. *Acta Materialia*. 2020, **186**, 172-189. ISSN 1359-6454. DOI:10.1016/j.actamat.2019.12.009
- [28] POLÁK, J. Electrical resistivity of cyclically deformed copper. *Czechoslovak Journal of Physics*. 1969, **19**(3), 315–322. ISSN 0011-4626. DOI:10.1007/BF01712868
- [29] MUGHRABI, H. Microstructural mechanisms of cyclic deformation, fatigue crack initiation and early crack growth. *Philosophical Transactions of the Royal Society A: Mathematical, Physical and Engineering Sciences*. 2015, **373**(2038). ISSN 1364-503X. DOI:10.1098/rsta.2014.0132
- [30] BABINSKÝ, T., I. KUBĚNA, I. ŠULÁK, T. KRUMML, J. TOBIÁŠ and J. POLÁK. Surface relief evolution and fatigue crack initiation in René 41 superalloy cycled at room temperature. *Materials Science and Engineering: A*. 2021, **819**. ISSN 0921-5093. DOI:10.1016/j.msea.2021.141520

## 7 List of publications by the author

### Publications related to the dissertation topic

**T. Babinský**, J. Polák, Effective and internal stresses in 713LC and Rene 41 superalloys using analysis of the hysteresis loop shape, *Procedia Structural Integrity*, 23 (2019) 523–528. <https://doi.org/10.1016/j.prostr.2020.01.139>.

**T. Babinský**, I. Kuběna, I. Šulák, T. Kruml, J. Tobiáš, J. Polák, Surface relief evolution and fatigue crack initiation in René 41 superalloy cycled at room temperature, *Materials Science & Engineering: A*, 819 (2021), <https://doi.org/10.1016/j.msea.2021.141520>.

### Other publications

**T. Babinský**, J. Dluhoš, A. Candeias, M. Petrevec, In-situ study of recrystallization and deformation processes in free-cutting steel, in: *Metal 2018 – 27th International Conference On Metallurgy And Materials, Conference Proceedings, Brno*, (2018) 35–39.

I. Šulák, K. Obrtlík, **T. Babinský**, S. Guth, The low cycle fatigue behaviour of MAR-M247 superalloy under different strain rates and cycle shapes at 750 °C, *International Journal of Fatigue*. 164 (2022). <https://doi.org/10.1016/j.ijfatigue.2022.107133>.

A. Chlupová, I. Šulák, **T. Babinský**, J. Polák, Intergranular fatigue crack initiation in polycrystalline copper, *Materials Science & Engineering: A*. 848 (2022). <https://doi.org/10.1016/j.msea.2022.143357>.

I. Šulák, **T. Babinský**, A. Chlupová, A. Milovanović, L. Náhlík, Effect of building direction and heat treatment on mechanical properties of Inconel 939 prepared by additive manufacturing, *Journal of Mechanical Science and Technology*, (2022). <https://doi.org/10.1007/s12206-022-2101-7>.

**T. Babinský**, I. Šulák, I. Kuběna, J. Man, A. Weiser, E. Švábenská, L. Englert, S. Guth, Thermomechanical fatigue of additively manufactured 316L steel, *Materials Science & Engineering: A*, 869 (2023), <https://doi.org/10.1016/j.msea.2023.144831>.